nuclear fusion
IAEA

PAPER • OPEN ACCESS

Studies of the boron erosion and deposition in shadowed areas in EAST

To cite this article: Yuming Liu *et al* 2025 *Nucl. Fusion* **65** 096024

OPEN ACCESS
IOP Publishing | International Atomic Energy Agency
Nuclear Fusion
Nucl. Fusion **65** (2025) 096024 (16pp)
https://doi.org/10.1088/1741-4326/adf8ff

Studies of the boron erosion and deposition in shadowed areas in EAST

Yuming Liu[1,2], Rong Yan[1,2,*], Lei Mu[1], Chuannan Xuan[1,2], Baoguo Wang[1], Yuqi Sheng[1,3], Zichao Lin[1,2], Ziqiang Zhou[1,2], Dahuan Zhu[1], Andrey Litnovsky[4] and Junling Chen[1]

[1] Institute of Plasma Physics, Hefei Institutes of Physical Science, Chinese Academy of Sciences, Hefei 230031, Anhui, China
[2] University of Science and Technology of China, Hefei 230026, Anhui, China
[3] Harbin Engineering University, Harbin 150001, Heilongjiang, China
[4] Forschungszentrum Jülich GmbH, Institute of Fusion Energy and Nuclear Waste Management (IFN-1), 52425 Jülich, Germany

E-mail: yanrong@ipp.ac.cn

Received 20 May 2025, revised 13 July 2025
Accepted for publication 7 August 2025
Published 20 August 2025

Abstract

Boronization is a widely employed technique for oxygen gettering and impurity suppression. It is expected to be an initial routine wall conditioning method for tungsten (W) plasma-facing components (PFCs) in ITER. To assess boron (B) performance under metal wall conditions, experimental campaigns with boronization were conducted in the Experimental Advanced Superconducting Tokamak. A quartz crystal microbalance installed at the mid-plane of port C (C-QMB), positioned 0.5 m behind the limiter, enabled *in-situ* monitoring of material erosion and deposition in magnetic shadowed areas during the wall conditioning processes and subsequent plasma discharges. Material erosion was detected in the majority (>50%) of discharges, regardless of whether they were normal plasma operations or terminated by disruptions. Transitions from erosion to deposition during normal discharges at the C-QMB have been shown to provide critical insights for estimating the lifetime of B-based coatings on nearby PFCs. Erosion rates were also found to be significantly influenced by the heating configuration. Electron cyclotron resonance heating (ECRH) discharges induced erosion rates 1.95 times higher than those in combined lower hybrid wave and ECRH discharges. Following a single boronization using 10 g of carborane, the B-based coating on C-QMB exhibited a lifetime of $\sim 10^4$ s under plasma exposure. Post-mortem analyses revealed that about 30 nm of a boron-carbon film remained on the C-QMB, demonstrating strong oxygen gettering capability and minor iron and copper contamination. This residual film exhibited a deuterium retention at a level of 2.12×10^{20} m^{-2}, more than eight times higher than that of pure W, highlighting the pronounced trapping capacity of B-containing films in low-flux regions. These results provide valuable insights into the application of boron in next-step devices such as ITER.

* Author to whom any correspondence should be addressed.

Keywords: boron, erosion and deposition, QMB, EAST

(Some figures may appear in colour only in the online journal)

Abbreviations

PFC	Plasma-Facing Component
QMB	Quartz crystal microbalance
MSA	Magnetic Shadowed Area
ECRH	Electron Cyclotron Resonance Heating
LHW	Lower Hybrid Wave
ELM	Edge Localized Mode
FW	First Wall
TZM	Titanium–Zirconium–Molybdenum
ICRF	Ion Cyclotron Range of Frequency
GD	Glow Discharge
ICRH	Ion Cyclotron Resonance Heating
NBI	Neutral Beam Injection
SEM	Scanning Electron Microscopy
EDS	Energy Dispersive Spectroscopy
XPS	X-ray Photoelectron Spectroscopy
FIB	Focused Ion Beam
TDS	Thermal Desorption Spectroscopy
UFO	Unidentified flying object
VUV	Vacuum Ultraviolet
AXUV	Absolute eXtreme UltraViolet
LFS	Low-Field-Side
EUV	Extreme Ultraviolet
LSN	Lower Single Null
LENPA	Low Energy Neutral Particle Analyzer
XCS	X-ray Crystal Spectroscopy
NRA	Nuclear Reaction Analysis

1. Introduction

Transport of impurities into core plasma during plasma-wall interactions can result in increased power radiation losses and degradation of plasma performance in fusion devices [1]. Finding an effective way to inhibit impurities from migrating into plasma has become a crucial task. Boronization [2] has proven effective in reducing particle recycling and preventing oxygen and other impurities from entering the plasma. It has been widely used in machines with carbon (C) [3, 4], molybdenum (Mo) [5–7], and tungsten (W) [8, 9] PFCs. Moreover, boronization will also become a routine initial wall conditioning method for the success of the ITER project, which will have a full W wall configuration according to the new baseline [10]. A comprehensive understanding of the erosion and deposition evolution of boron (B) is essential to evaluate the application of boronization in fusion devices. Significant efforts have been made to study boron erosion and deposition in fusion devices, such as ASDEX Upgrade [11, 12], RFX [13–15], Globus-M [16], and TEXTOR [17], typically based on post-mortem material analysis after experimental campaigns. The study in ASDEX Upgrade has revealed that boron films were deposited mainly in the main chamber, from which they were eroded and redeposited in the divertor regions [11]. Boron has also been found in the MSA of the divertor in Globus-M [16] and in gaps of the main toroidal limiter in TEXTOR [17], with a significant amount of deuterium (D). Fuel retention in boron co-deposits in the MSAs is a major concern for burning plasma operations, as it can cause safety and fuel cycle issues [18, 19]. Therefore, real-time studies of boron film erosion and deposition behavior in MSA play an important role in understanding the hydrogen (H) isotope retention. The QMB diagnostic system, which is based on the piezoelectric effect, enables *in-situ* and real-time measurements of material erosion and deposition with a high mass resolution of ng $\times$ cm^{-2}. Its results have shown good agreement with post-mortem ion beam analysis [20], making QMB a reliable tool for studying plasma-wall interactions. QMBs have been widely used in Alcator C-Mod [21], NSTX [22], JET [23], and Experimental Advanced Superconducting Tokamak (EAST) [24]. In NSTX, QMBs located in MSAs at the outer divertor and vessel wall, exhibited a complex temporal pattern of mass gain and loss [22]. Studies in JET demonstrated that ELMs enhanced erosion of carbon-deuterium co-deposits in a nonlinear manner, prompting accelerated material dislocation towards shadowed areas [23].

EAST is a fully superconducting tokamak equipped with tungsten upper and lower divertor. Since 2021 the plasma-facing FW is made from TZM alloy containing 99 wt.% of Mo. The boronization technique, employing carborane ($C_2B_{10}H_{12}$) as a boron source and assisted by ICRF plasma has been developed [25, 26]. During the 2021 EAST campaign, material deposition and erosion rates during wall conditioning processes [27] and plasma discharges [28] were successfully measured by QMBs. The results revealed that during lithium (Li) coating, material deposition was strongly influenced by the location of the Li oven [27]. In normal plasma discharges, net erosion was found to be predominant, whereas in disruptive discharges, the proportion of net erosion cases decreased significantly [28].

During the EAST 2024 spring experimental campaign, a QMB system located at the mid-plane of port C 0.5 m away from the FW has been developed. A 50 nm W coating was adopted on the QMB sensors to study the boron evolution behavior in EAST with metal wall environment. This paper reports on the evolution of B-based material erosion and deposition in MSA during the 2024 spring campaign (from 20 February 2024 to 4 May 2024) in EAST. Section 2 introduces the boronization process in EAST tokamak, plasma exposure conditions, the QMB diagnostic, and post-mortem analysis methods. Section 3.1 discusses the evolution of B-based material erosion and deposition during plasma operation, while section 3.2 investigates the distinct erosion–deposition transitions observed during normal plasma operation. The influence of different heating configurations on the erosion of B-based films is examined in section 3.3. Section 3.4 presents

the results of post-mortem analyses. The main conclusions and outlook are summarized in section 4.

2. Experimental setup

2.1. Boronization

Nine boronizations were carried out during the 2024 spring campaign. These boronizations are designated as B1 to B9 correspondingly. Boronizations B1 to B7 employed D_2 ICRF plasma, while B8 and B9 utilized D_2 GD plasma. For ICRF-assisted boronizations, a toroidal magnetic field of 0.5 T and a working pressure of 0.05 Pa were applied. As shown in figure 1, two ICRF antennas were used: one located between ports A and B (A-B), and the other between ports I and J (I-J). During B1, both antennas were operated at a power of 55 kW, while for B2 to B7, the A-B antenna was set to 30 kW, and the I-J antenna power varied between 20 kW (B2-B6) and 15 kW (B7). In contrast, GD-assisted boronizations were performed without a magnetic field and at a higher working pressure of 0.5 Pa. In B8 three anodes were employed, located at ports P and A (P-A), F and G (F-G), and J and K (J-K), while B9 used two anodes at ports P-A and F-G (figure 1). In both cases, each anode operated at an average power of approximately 400 W (2 A, 200 V).

The boronization process was conducted with the FW maintained at approximately room temperature. Each boronization began with a 0.5–3 h pre-cleaning using ICRF or GD plasma to remove surface impurities. The F oven, loaded with 5 g of carborane, was inserted at a major radius of 1.9 m and heated to 80 °C–100 °C, enabling carborane volatilization. The volatilized carborane was then ionized in the plasma, initiating the coating. After complete evaporation, the F oven was retracted, and the O oven (also containing 5 g of carborane), was inserted to perform an identical process. Following the coating, a 0.5–2 h post-cleaning using ICRF or GD plasma was performed to reduce hydrogen retention in the deposited B-rich layer. It should be noted that ICRF cleaning was routinely performed overnight following daytime plasma discharges, regardless of whether boronization took place.

2.2. Plasma exposure

EAST is equipped with several different auxiliary heating systems, including 10 MW of LHW (4 MW at 2.45 GHz of LHW1 and 6 MW at 4.6 GHz of LHW2), 3 MW of ECRH, 12 MW of ICRH, and 4 MW of NBI in both co- and counter-current configurations [29]. The locations of auxiliary heating systems are shown in figure 1.

The 2024 spring campaign, conducted from 20 February to 4 May, lasted 74 d. After the first boronization, a total of 3865 plasma discharges were carried out, including 2505 normal and 1360 disruptive shots, with a total plasma duration of 40 497.49 s. Test discharges conducted every morning without plasma initiation were excluded from the statistics. The plasma initiation was primarily achieved through EC pre-ionization, with subsequent heating typically provided by either pure ECRH or a combined approach utilizing both LHW and ECRH. To investigate the effects of heating configurations on B-based material erosion, plasma operations conducted on the first day after each boronization were selected. Among normal discharges on these days, approximately 34% employed pure ECRH, while 38% utilized a combination of LHW2 and ECRH. The ECRH power ranged from 0.6 to 3 MW, whereas LHW2 power ranged from 0.5 to 2.2 MW. The line-averaged electron density (n_e) was ranging from 1 to 6×10^{19} m^{-3}. The plasma current (I_p) ranged from 250 to 500 kA.

2.3. QMB system

A QMB system was installed at the mid-plane of port C (C-QMB) at the major radius of 2.85 m (0.5 m behind the limiter), as shown in figure 1. The system comprises two sensors (working and reference), dual oscillators, a water-cooling system, a vacuum feedthrough, and a controller [24, 27]. The working sensor, oriented directly toward the plasma, detects changes in resonant frequency due to material erosion or deposition. In contrast, the reference sensor is shielded by a Mo baffle to protect it from plasma exposure. This dual-sensor configuration effectively minimizes the interference from environmental factors, such as temperature and radiation. Both sensors were equipped with full-pad gold (Au) electrodes with a diameter of 14 mm and a thickness of 300 nm for electrical conductivity. A ∼20 nm chromium (Cr) film was employed as a cohesion layer between the quartz substrate and Au electrode. During the 2024 spring campaign, the sensors were coated with a 50 nm W film of 8 mm diameter, consistent with the FW material proposed for ITER.

The QMB system was used to monitor mass changes during boronization, cleaning processes and plasma discharges in the EAST campaign. Mass change was derived from the differential frequency shift between the two crystals, following a linear relationship as described by the Sauerbrey equation [30]. Data collection was temporarily interrupted from 15–26 March 2024, due to an oscillator failure, with normal data acquisition resuming after its replacement on 26 March 2024. Beyond this period, the QMB data showed no abnormal drift or interruptions.

2.4. Samples characterization

Before and after the campaign, the SEM measurement was carried out to check the morphology of the QMB sensor surface on a field-emission SU8020 Hitachi SEM coupled with (OXFORD X-Max^N). Following the campaign, XPS result was obtained to analyze the elementary composition and assess the impurity levels by a Thermo ESCALAB250Xi spectrometer with an excitation source of monochromatized Al Ka ($hv = 1486.6$ eV) and a pass energy of 30 eV. Cross-sectional imaging of the sensor was performed using a Helios G4 UX focused Ga^+ ion beam-scanning electron microscope (FIB-SEM). Besides, TDS was used to quantify the deuterium retention behavior of the QMB sensor. During the TDS measurement, the QMB sensor was heated in a quartz tube under a typical vacuum background pressure of about 1×10^{-5} Pa, from room temperature to 1000 °C at a ramping rate of 10 °C min^{-1}.

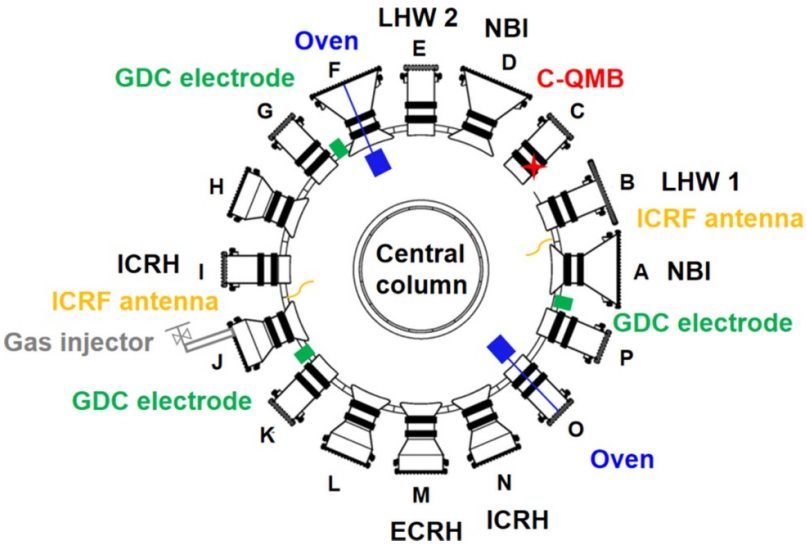

Figure 1. Toroidal locations of the ovens, ICRF antennas, GDC electrodes, the gas inlet, auxiliary heating systems, and C-QMB.

The released D_2 and HD signals were detected using a quadrupole mass spectrometer, and the total amount of D released was calculated by adding twice the amount of D_2 to the amount of HD signals.

3. Results and discussion

3.1. Material erosion and deposition evolution during plasma discharges

Figure 2(*a*) shows the temporal evolution of the accumulated frequency and corresponding mass change recorded by the C-QMB for plasma discharges following the first boronization of the 2024 spring campaign. These discharges are categorized into three types: normal, disruptive, and total. The timing of nine boronization events (B1-B9) is marked by green dashed lines. Due to an oscillator malfunction, C-QMB measurements were unavailable for several days around B2 and the results are therefore not shown. During the most normal discharges, the accumulated frequency exhibited a continuous increase, indicating net erosion of the B-based layer. However, intermittent transitions to deposition were occasionally observed, likely due to the complete erosion of the local B-based coating. This will be discussed in more detail in section 3.2. Disruptive discharges also showed a general trend of net erosion. However, a distinct deposition event was observed between B2 and B3, corresponding to several disruptive shots with large mass accumulation. This anomaly likely resulted from unstable plasma conditions during recovery shots following the LHW limiter water leakage, which may have influenced impurity transport and deposition behavior. Since the 'all shots' category encompassed both normal and disruptive discharges, its accumulation curve reflects a composite of both behaviors.

To further illustrate erosion and deposition across individual discharges, figure 2(*b*) presents a histogram of mass changes for each discharge. Among normal discharges, 69% exhibited net erosion and 31% net deposition, with 72% of the discharges showing mass changes below 6.2 ng cm^{-2}. A comparable outcome was noted for disruptive discharges: 61% demonstrated net erosion, while 39% exhibited deposition, with 83% remaining below 6.2 ng cm^{-2}. This behavior contrasts with previous studies on aluminum (Al) substrates, where disruptive discharges more frequently resulted in net deposition [28, 31]. This discrepancy may be attributed to differences in the reflection coefficients of the D or B atoms on different substrate materials (Al and W). Specifically, the reflection coefficient of a light projectile particle increases with the atomic number of the target [32, 33]. As such, the reflection rate for D or B on W is higher than on Al. The elevated reflection coefficient on W results in a greater proportion of incident atoms being reflected back into the plasma rather than being incorporated into the deposited film, thereby promoting net erosion. However, it should be noted that when the B film is thin, energetic particles can partially penetrate and interact with the W substrate, causing enhanced reflection and reduced deposition. As the B layer thickens, the influence of the underlying substrate diminishes, and the surface behavior is dominated by the properties of the B film itself rather than the substrate material. This is consistent with our observations, as erosion during disruptive discharges decreased in the later phase of the campaign. Uncontrolled disruptions pose a serious threat to PFCs, as excessive high particle and heat fluxes can strike the wall and cause significant damage [34]. Material migration under such conditions is a highly complex process involving dynamic interactions between transient loads and surface materials. It is evident that further investigation is required to elucidate the interplay behavior and to develop effective mitigation strategies [35, 36].

Table 1 summarizes the overall exposure results for the C-QMB. The total net erosion over the campaign was 6.45 μg cm^{-2} (524.77 Hz), with 5.30 μg cm^{-2} (431.29 Hz) from normal discharges and 1.15 μg cm^{-2} (93.48 Hz) from

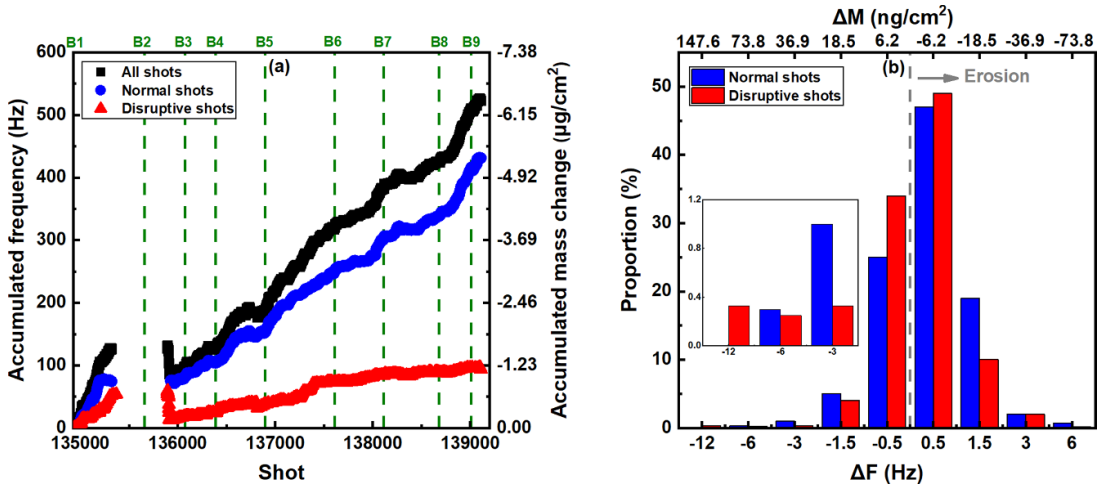

Figure 2. (*a*) Temporal evolution of accumulated frequency and mass change for the C-QMB during normal, disruptive plasma discharges following the first boronization in the 2024 spring experimental campaign. (The green dashed line indicates the boronization during the campaign.), (*b*) the erosion and deposition distribution for C-QMB. (The insert shows a magnified view of specific regions of the histogram, utilizing the same *x* and *y*-axes as the main figure).

Table 1. General exposure results of erosion and deposition of C-QMB in EAST. (Exposure time excludes plasma discharges during oscillator malfunction periods).

Discharge	Shot number	Exposure time	Net erosion (μg cm^{-2})	Average erosion rate (ng cm^{-2} s^{-1})
Total	3346	34 791.7	6.45	0.19
Normal	2147	28 184.3	5.30	0.19
Disruptive	1199	6607.4	1.15	0.17

disruptive discharges. Due to the non-defined flat-top duration in many disruptive shots, total shot length rather than flat-top duration was used to calculate erosion rates. The average erosion rate was estimated at 0.19 ng cm^{-2} s^{-1} for normal discharges and 0.17 ng cm^{-2} s^{-1} for disruptive discharges, yielding an overall campaign average of 0.19 ng cm^{-2} s^{-1}.

The amount of B-based material deposited during the boronization process varies depending on factors such as plasma parameters [37]. Four representative boronization events with consistent key parameters, including 10 g of carborane injected (5 g through each of ports F and O) under radiofrequency power of 20 kW from the I-J ICRF antenna and 30 kW from the A-B antenna, were selected. Under these conditions, the measured B-based loading on the C-QMB ranged from 1.29 to 2.52 μg cm^{-2}, with an average value of 1.79 μg cm^{-2} and a standard deviation of 0.54 μg cm^{-2}. These variations are likely attributed to differences in oven temperature, FW temperature, and boronization duration (ranging between 2 and 3 h), all of which influence the amount of boron deposited [38]. Based on the average initial deposition and the average total erosion rate (excluding wall cleaning effects such as GD or ICRF cleaning), the estimated coating lifetime on the C-QMB was 9421 s, about five times longer than that on the FW (∼2000 s, equivalent to ∼150 discharges of 15 s each, 3–4 d of regular operation) [39]. Considering the observed variation in B-based loading, the coating lifetime may range from 6789 s to 13 263 s, reflecting the minimum and maximum deposition values measured. The extended lifetime of B-based coatings in shadowed regions observed in our study is consistent with WallDYN simulations for ITER, which predict significantly prolonged boron lifetimes in recessed areas due to limited ion bombardment and erosion dominated by charge-exchange neutrals, reaching the order of 10^5 s [40]. Future work will incorporate simulations such as WallDYN or ERO combined with EAST experimental data to enable cross-validation and improve understanding of material migration and retention behaviors.

Net material deposition was also observed on the C-QMB during overnight ICRF wall conditioning, which was conducted between routine daytime plasma operations. This process contributed an average deposition of about 0.1 μg cm^{-2} per cleaning cycle. A similar result was reported in KSTAR [41], which employed carborane for boronization as well. In that case, net deposition was detected on QMBs located within the diagnostic duct during GD wall cleaning. These observations indicate that, while wall conditioning processes are effective for PFCs, they can also lead to material accumulation in MSAs, such as diagnostic mirrors. Such deposition may progressively degrade optical performance and diagnostic accuracy, and should therefore be carefully considered in device operation and engineering design [42]. Taking into account the additional deposition during wall conditioning, the effective

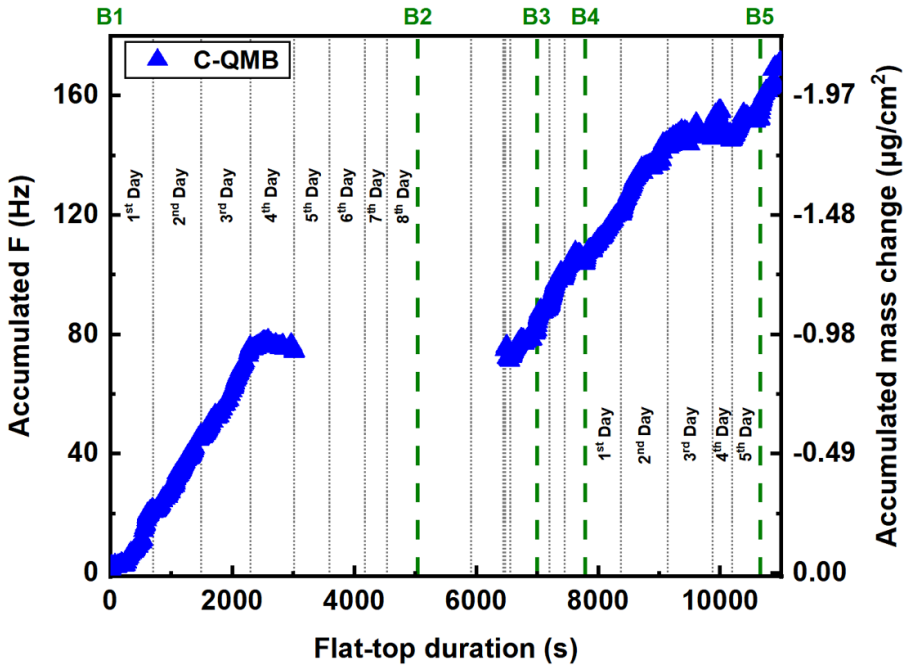

Figure 3. Temporal evolution of accumulated frequency and mass change for C-QMB under full discharges between Shot 134940 and 136940 during 2024 spring campaign. (The green dashed line indicates the boronization during the campaign. The '1st day' represents the first day after boronization, and so on.).

lifetime of B-based coatings on the C-QMB could extend from the average estimated lifetime of 9421 s to the order of 10^4 s.

The extended persistence of B-based coatings may pose both benefits and challenges to EAST's weekly boronization schedule. While typical discharge durations (∼5000 s) help to sustain oxygen gettering between boronizations, the gradual accumulation of boron raises concerns regarding H isotope retention [10, 43] and potential plasma disruption [19, 44]. Previous studies have reported that thick deposits formed in the shadowed regions are associated with the frequent release of UFOs (large impurity particles with a high impurity content), which have triggered plasma detachment phases and subsequent disruptions in several instances [44]. Although the QMB is far from the limiter, some shadowed regions near the limiter may also have thicker boron deposits, which could increase the risk of such events in those areas. Therefore, plasma operation and wall conditioning strategies must carefully balance the need for effective oxygen gettering against the risk of excessive B-based material accumulation in MSAs.

3.2. Distinct erosion-deposition transition in normal discharges

As noted in section 3.1, intermittent transitions to net deposition were observed during normal discharges. To investigate such a behavior in detail, we will focus on normal discharges between shots #134940 and #136940, during which distinct erosion-to-deposition transitions were consistently observed several days after boronization. Figure 3 presents the temporal evolution of the accumulated frequency and mass change measured by the C-QMB during these discharges. The timing of five boronization events (B1-B5) is denoted by green dashed lines, with the first plasma operation day following each event designated as '1st day'. A marked transition in erosion behavior occurred after B1, with the C-QMB shifting from an erosion-dominated to a deposition-dominated regime on the 4th day. Notably, a similar erosion-to-deposition transition was observed on the 3rd day following B4.

To examine the transition observed after B1 in more detail, four representative discharges (#134977, #135060, #135148, and #135216) were analyzed, corresponding to the 1st to 4th day post-B1. These discharges were carried out under identical plasma parameters (I_p = 400 kA, $n_e = 4 \times 10^{19}$ m^{-3}) and heating configurations (3 MW ECRH and 2 MW LHW at 4.6 GHz). The C-QMB recorded erosion rates of 0.21, 0.20, and 0.30 ng cm^{-2} s^{-1} on days one to three, respectively, which transitioned to a net deposition rate of 0.14 ng cm^{-2} s^{-1} on the fourth day. The evolution of plasma parameters, edge boron content, and both core and edge radiation power associated with these discharges is summarized in figure 4.

The temporal change in boron concentration at the plasma boundary was characterized using VUV spectroscopy, specifically through measurements of B II emission at 162.4 nm. A progressive decline in boron content was observed across the four days, except for #134977, for which spectroscopic measurements were not performed. Concurrently, a steady increase in both core and edge radiation power measured by AXUV diagnostic systems was recorded, indicating elevated impurity content [45]. This behavior is consistent with the known erosion of boron films during plasma operation and their diminishing effectiveness in impurity suppression over time [12]. As the protective capabilities of the B-rich coating degrade, sputtering from various PFCs, including the FW, divertor, heating antennas, and LFS diagnostics, becomes

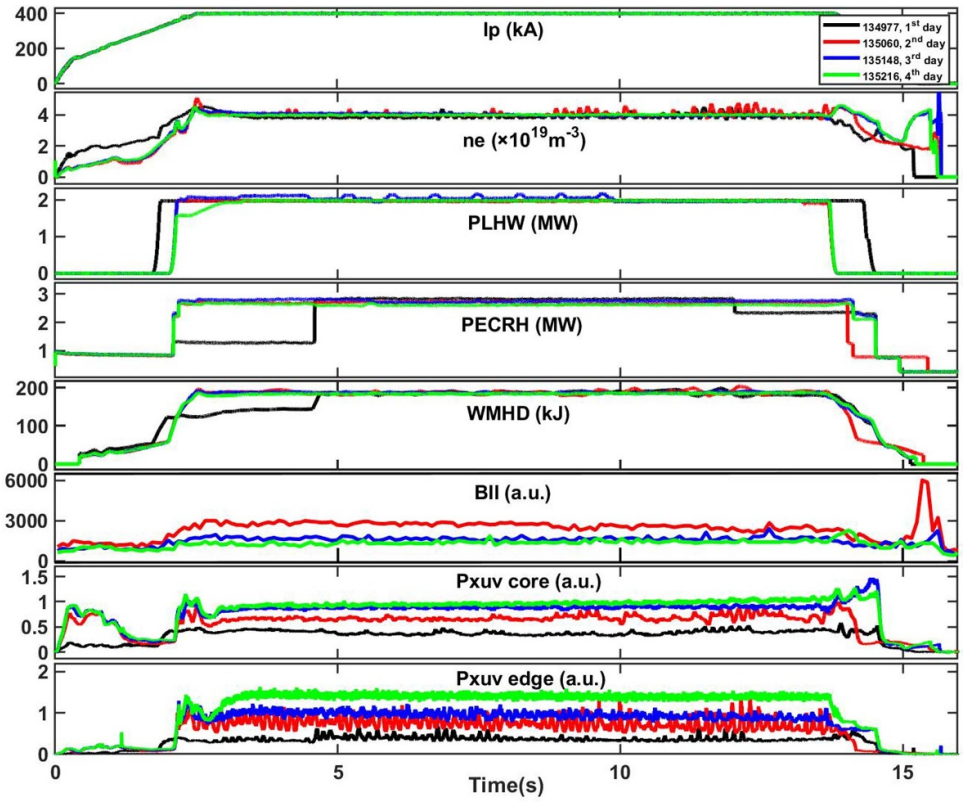

Figure 4. Temporal evolution of B II (162.4 nm) emission intensity measured by vacuum ultraviolet (VUV) spectroscopy and radiation power loss in plasma core and edge after boronization B1.

more pronounced. This leads to increased material redeposition onto the C-QMB. Although high-Z impurities such as W and Mo from distant components (e.g. divertor or FW) tend to undergo local redeposition [46, 47], the material accumulating on the C-QMB appears to originate primarily from nearby structures such as the copper (Cu) LHW antenna and adjacent stainless-steel diagnostic components [48]. This interpretation is further supported by EDS and XPS analyses discussed in section 3.4.

Additional evidence is provided by EUV spectroscopy, which revealed elevated levels of iron (Fe) and Cu impurities in the plasma core on the third day after B4, with concentrations of Cu and Fe approaching those of an uncoated metal wall [39]. This coincides with a similar erosion-to-deposition transition observed on the same day, underlining the proposed correlation between boron coverage degradation and impurity-driven material migration. These observations highlight the pivotal role of impurity accumulation and transport in governing the erosion-deposition balance at the C-QMB. Essentially, they demonstrate that time-resolved erosion rate measurements via C-QMB offer a sensitive and quantitative method to evaluate the effective lifetime of b-based coatings on nearby PFCs under repeated plasma exposure in a tokamak environment.

3.3. Material erosion and deposition rates under different heating configurations

Boronization is routinely performed in EAST on a weekly basis, after which the FW undergoes complex plasma-wall interactions, gradually forming mixed-material surfaces. This section focuses on the erosion and deposition dynamics of freshly deposited B-based films using QMB data collected during the first plasma operation day following boronization, providing insights into the behavior of pristine B-rich layers under different heating configurations.

Figure 5 illustrates the erosion behavior of B-based material under two heating configurations: (1) combined LHW and ECRH, with LHW applied at 4.6 GHz and a power of 1.8–2.2 MW together with 3 MW ECRH; and (2) ECRH-only at 3 MW. Both configurations were operated at a plasma current of 400 kA. In figure 5(*a*), the accumulated frequency measured by C-QMB is plotted against shot number, with all discharges sorted by n_e within the range of 3.5–4.5 $\times$ 10^{19} m^{-3}. A total of 66 discharges were analyzed for the LHW + ECRH condition and 54 for the ECRH-only condition. A steeper increase in frequency accumulation was observed under the ECRH-only configuration, reaching 15.48 Hz in total, compared to 12.71 Hz for the LHW-assisted configuration. This suggests a

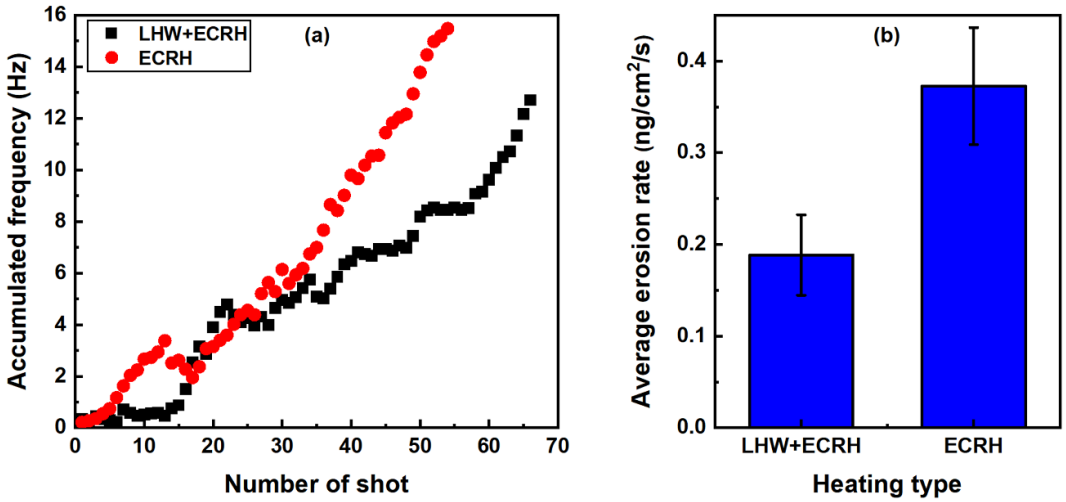

Figure 5. Erosion patterns of B-based material in C-QMB under different heating methods. (*a*) Accumulated frequency as a function of shot number, with discharges sorted by increasing plasma density for LHW + ECRH (black) and ECRH-only (red). (*b*) Average erosion rates for the two configurations. Data obtained from discharges with similar conditions: $I_p = 400$ kA, $n_e = (3.5–4.5) \times 10^{19}$ m^{-3}, PECRH = 3.0 MW, PLHW2 = 1.8–2.2 MW.

higher occurrence of net erosion events when LHW is absent. Quantitative erosion rates extracted from C-QMB are shown in figure 5(*b*). The average erosion rate in the ECRH-only condition was 0.37 ± 0.06 ng cm^{-2} s^{-1}, approximately 1.95 times higher than that observed under the LHW + ECRH scenario (0.19 ± 0.04 ng cm^{-2} s^{-1}). Error bars represent the standard error of the mean.

To clarify the mechanisms behind this difference, we conducted a detailed comparison of two representative discharges (#136954 and #137621), both with identical baseline plasma parameters ($I_p = 400$ kA and $n_e = 4 \times 10^{19}$ m^{-3}) and a LSN magnetic configuration. Discharge #137621 employed 3 MW of ECRH, while #136954 utilized combined heating with 3 MW ECRH and 2 MW LHW at 4.6 GHz. The fueling rates were 2.60×10^{20} D/s for discharge #137621 and 6.98×10^{20} D/s for #136954. As shown in figure 6, the addition of LHW led to a 22.67% increase in stored energy (from 150 kJ to 184 kJ) and a 3.53-fold enhancement in edge radiation power (from 0.30 to 1.06), indicating substantial changes in boundary plasma conditions.

Further insights were gained from LENPA measurements of the neutral particle characteristics, presented in figure 7. Compared to the LHW + ECRH case, the ECRH-only discharge exhibited an 86% higher neutral particle flux (particularly in the 500–3000 eV range) and an 84% increase in mean energy. These enhancements are consistent with the observed increase in erosion under ECRH-only conditions and suggest that both elevated sputtering by charge-exchange neutrals and reduced edge radiation, which would otherwise favor redeposition, contributed to the higher erosion levels [28].

To understand the origin of this difference in neutral behavior, ion temperature (T_i) and n_e profiles were analyzed. As shown in figure 8(*a*), XCS measurements revealed that core ion temperature in the LHW + ECRH discharge was ~10% lower than that in the ECRH-only case. Although direct measurements of T_i at the plasma edge are not available in EAST, a more pronounced reduction is expected in the boundary region where cold fueling particles are injected, due to enhanced local cooling and charge-exchange processes associated with the higher fueling rate [49, 50]. Such a decrease would shift the Maxwellian ion velocity distribution toward lower energies, causing more charge-exchange neutrals to fall below the LENPA detection range (20–3000 eV) [51, 52]. Simultaneously, as shown in figure 8(*b*), the higher electron density observed in the LHW + ECRH discharge, as measured by microwave reflectometer system, increases the probability of ionization and charge exchange collisions. These enhanced collisional processes contribute to both the attenuation of the neutral flux and a reduction in their mean energy before reaching the wall, primarily through increased ionization loss and energy degradation via multi-step charge exchange [53, 54].

While T_i and n_e profiles explain the observed difference in neutral behavior, other factors related to the distinct power deposition characteristics and wave-plasma interaction physics of the different heating scenarios may also play a role. In particular, the variation in fueling rates between the discharges complicates the interpretation of these effects. Detailed physical analysis is in process by designing controlled experiments combined with modeling efforts [55]. Notably, the localized central heating provided by ECRH is expected to suppress W accumulation in the plasma core. Therefore, in the ITER new baseline, an increase in ECRH power during the initial operational phase is deemed necessary [56]. However, the elevated flux and energy of low-energy neutrals observed under ECRH-only conditions may enhance neutral-induced sputtering, potentially reducing the lifetime of PFCs. This issue requires careful assessment while planning the design and operational environment of future devices.

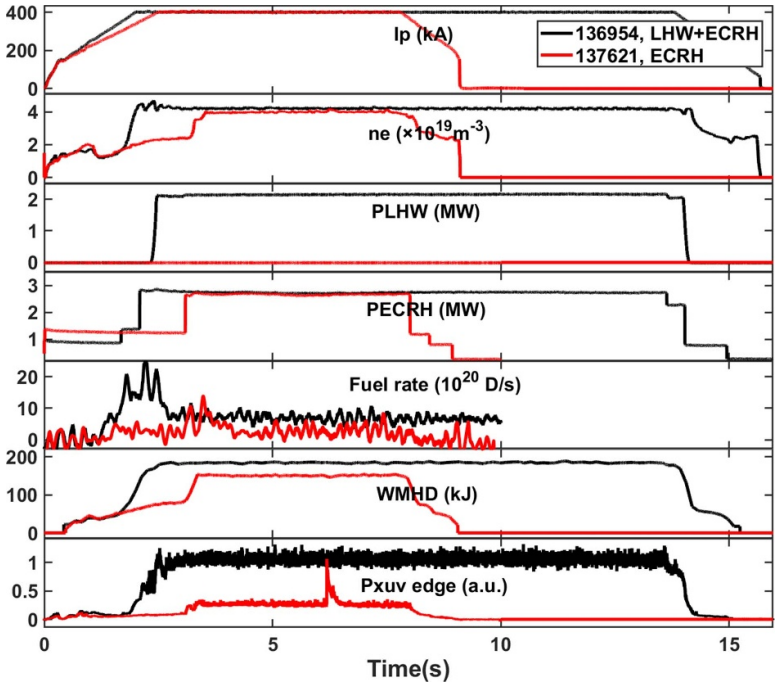

Figure 6. Typical parameters for discharges #136954 (LHW + ECRH, black) and #137621 (ECRH, red), such as plasma current (I_p), line-averaged electron density (n_e), fueling rate (Fuel rate), heating power from LHW at 4.6 GHz (PLHW), heating power from ECRH (PECRH), plasma stored energy (WMHD), and line integrated radiation power along edge chord (Pxuv edge).

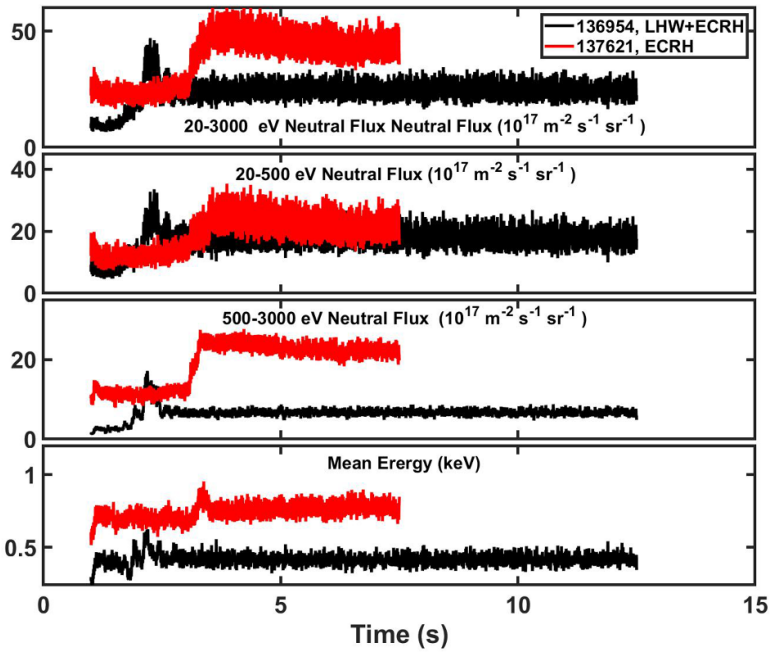

Figure 7. Neutral flux and mean energy for discharges #136954 (LHW + ECRH, black) and #137621 (ECRH, red) measured by low-energy neutral particle analyzer (LENPA).

3.4. Post-mortem analysis of QMB sensor

3.4.1. Morphology and composition. Post-mortem analysis was conducted to investigate the surface characteristics of the C-QMB working sensor after it was removed following the EAST 2024 spring campaign. As shown in figure 9(*b*), the sensor surface exhibited a hazy morphology, in contrast to the well-defined granular structure observed before the campaign (figure 9(*a*)). This morphological change may be attributed to the formation of a thin amorphous overlayer, which filled and leveled the original surface microstructures [43, 57].

Elemental composition analysis, determined by EDS using a 5 keV electron beam, revealed that the surface composition of the original sensor consisted of 66.49 at% W, 27.67 at%

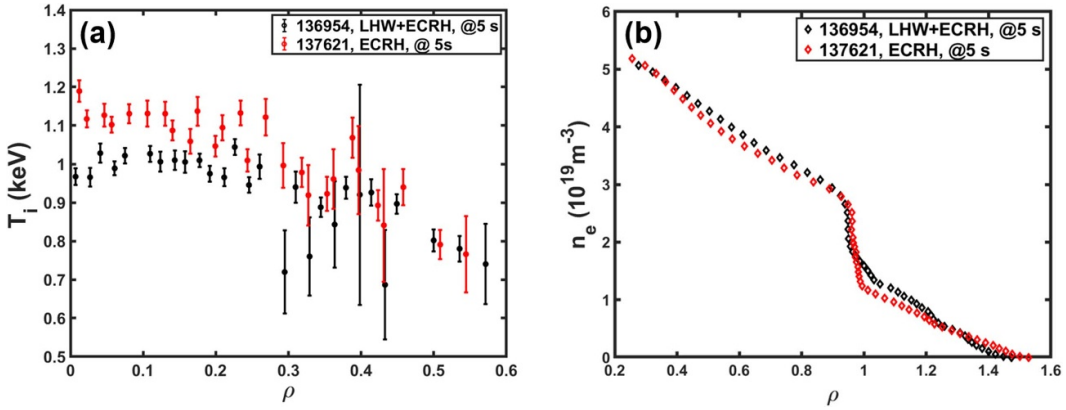

Figure 8. Comparison of plasma ion temperature (T_i), and electron density (n_e) profiles at $t = 5.0$ s for discharges #136954 (LHW + ECRH, black) and #137621 (ECRH, red), (*a*) T_i profiles provided by x-ray crystal spectroscopy, (*b*) n_e profiles provided by microwave reflectometer system.

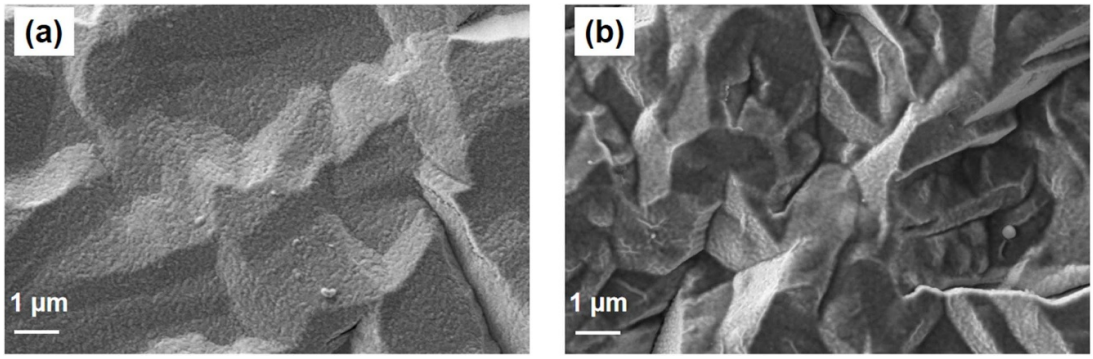

Figure 9. Surface morphology of QMB working sensor (*a*) before and (*b*) after the 2024 spring campaign in EAST.

O, and 5.84 at% Au, corresponding to the W coating and Au electrode. After the campaign, significant surface modification was observed: the W content decreased to 24.62 at%, and Au was no longer detectable, indicating coverage by a newly deposited layer. A B-rich surface layer was identified, composed of 30.47 at% B, along with elevated concentrations of O (28.17 at%) and C (11.17 at%). The predominance of B, C, and O is consistent with previous observations from HT-7 [58], further supporting the formation of amorphous boron-carbon a-B/C:H films. The boron originated from the carborane precursor used in the boronization process. The carbon was likely derived from both the precursor and the redeposition of eroded graphite impurities from the high-field side FW (doped graphite tiles used as NBI target components). In addition, trace amounts of Fe (4.85 at%) and Cu (0.72 at%) were detected, despite being absent from the original sensor composition. Their presence supports the inference proposed in section 3.2, where the erosion-to-deposition transition was attributed to redeposition from the adjacent stainless-steel components and the LHW antenna once the B-based coating had been depleted.

3.4.2. Composition depth profile and thickness. Figure 10 presents the elemental composition of the modified layers on the QMB working sensor, as measured by XPS, with sputtering time serving as a relative depth scale in the absence of calibrated sputtering rates. At the surface, the carbon concentration was notably high (∼36.2 at%), indicating surface contamination. As sputtering proceeded, the carbon concentration decreased significantly, reaching ∼12.5 at% after 1 min and remaining relatively stable (10.6–13.4 at%) at greater depths. Concurrently, the boron concentration increased from ∼29.9 at% at the surface to a peak of 44.9 at% at 6 min of sputtering, followed by a gradual decline. Signals from the underlying W substrate began to emerge between 6 and 8 min of sputtering. However, the sputtering duration was insufficient to achieve full exposure of the pure W substrate. The oxygen concentrations remained consistently high throughout the profile, ranging from 28.1 at% to 38.6 at%. Metallic impurities, including Fe (2.5–6.2 at%), Cu (1.1–2.8 at%), Mo (0.5–1.3 at%), and Ni (0.4–1.1 at%), were relatively low and showed minimal variation with depth.

To further investigate the chemical bonding states within the B-based layer, XPS spectra of the B 1 s and C 1 s regions were analyzed after 1 min of sputtering, as shown in figure 11. Figure 11(*a*) shows the B 1 s spectrum, revealing the presence of B–B bonds (188.4 eV), B–C bonds (189.8 eV), B–O bonds (191.8 eV), and B_2O_3 (193.2 eV) [59–63]. Figure 11(*b*) presents the C 1 s spectrum, which exhibits C–B bonds (283.3 eV), C–C bonds (284.8 eV), and C–O bonds (286.7 eV)

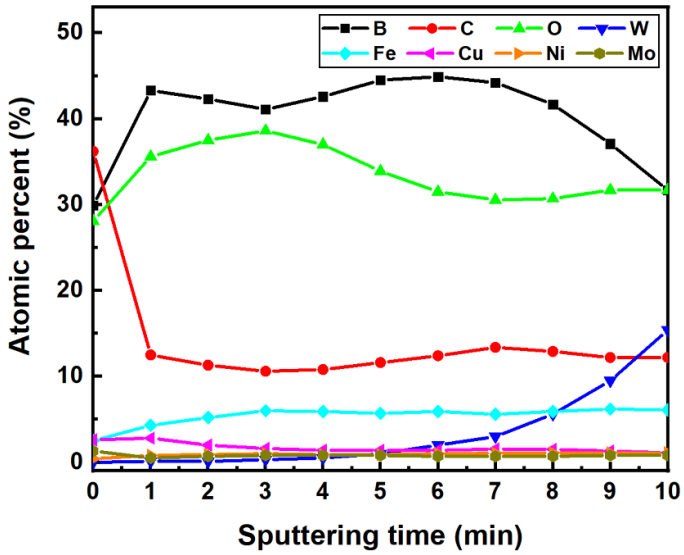

Figure 10. Elemental composition depth profile of the working sensor measured by XPS using Ar ion sputtering.

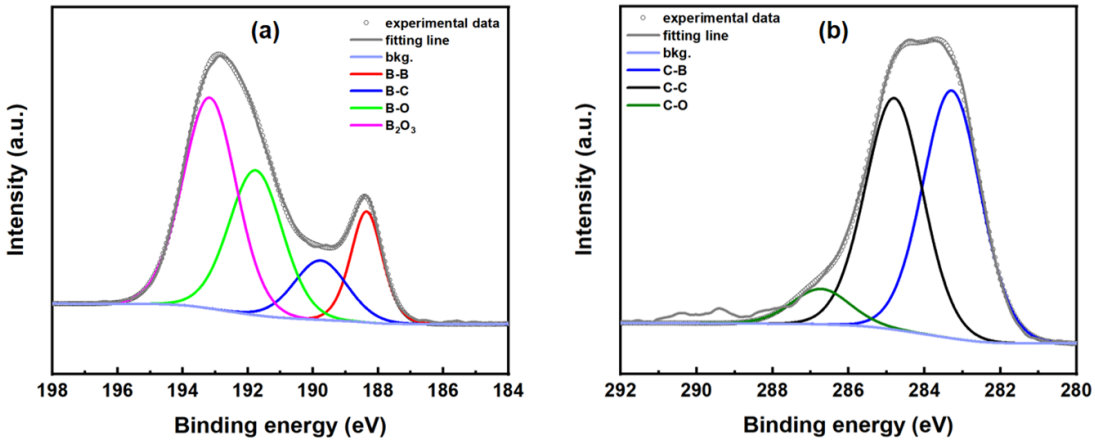

Figure 11. XPS spectra of the (*a*) B 1 s and (*b*) C 1 s regions of the working sensor, along with peak fitting results. The XPS profiles were measured after sputtering for 1 min.

[59]. It should be noted that the B 1 s peaks appeared slightly shifted toward higher binding energies compared to those of pure boron phases, which may suggest the possible involvement of deuterium within the bonding environments [61, 62].

Although surface contamination was present, the deeper regions (corresponding to sputtering times between 1 and 8 min) provided more reliable compositional information. The B/C atomic ratio of the QMB sensor was found to be about 3.6, which is consistent with the expected values for films produced from carborane precursors [64, 65]. In contrast, a comparison with the shadowed region deposits from Globus-M, which also employed carborane as the boronization procedure, revealed significant differences [16]. In Globus-M, the boron concentration was approximately 57% of the carbon content, as determined by NRA. This discrepancy can likely be attributed to differences in plasma discharge conditions and FW materials. Specifically, Globus-M employed recrystallized graphite doped with titanium (RGTi), whereas EAST utilizes a metal wall configuration. Moreover, the O/B ratio in the QMB sensor was about 0.8, which aligns with findings from W7-X [66], where samples exposed during individual boronization cycles on the multi-purpose manipulator exhibited an O/B ratio between 0.5 and 0.9. This consistency suggests that the B-based film on the MSA also demonstrated effective oxygen gettering ability.

Further post-mortem FIB-SEM characterization, shown in figure 12, revealed that the deposits on the W coating were dense, with no evidence of flaking. Quantitative analysis determined that the deposited B-based layer had a thickness of 29.09 nm. Considering the influence of data gaps, throughout the boronization phases, the C-QMB accumulated 13.39 μg cm^{-2} of B-based material. During the wall conditioning, the C-QMB received an additional 4.92 μg cm^{-2} of deposition. Subsequent plasma operation induced net erosion of 7.38 μg cm^{-2} ($\sim$600 Hz) on the C-QMB, resulting in residual B-based inventories of 10.93 μg cm^{-2}. When converted to geometric thickness using a nominal density of 1.6 g cm^{-3} for a-B/C:H films, assumed in this study based on values reported

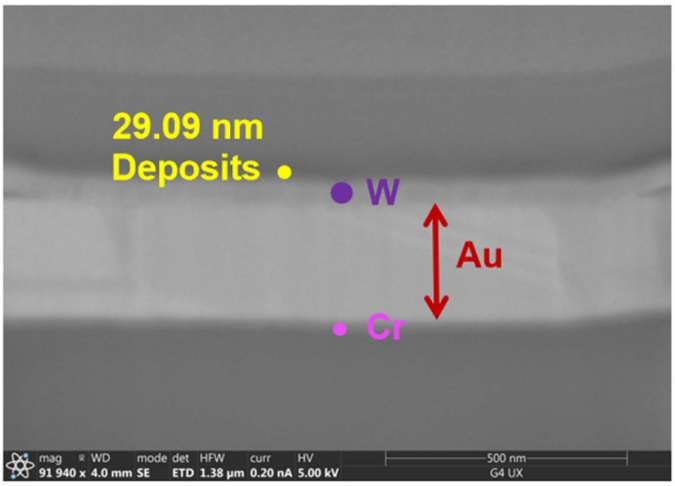

Figure 12. Cross-sectional imaging of the working sensor measured by FIB-SEM.

for B-containing films deposited from carborane [64, 65] and densities used in NSTX boronization studies [67, 68], the residual layers correspond to a thickness of 68.31 nm on the C-QMB. Discrepancies between the QMB-derived and FIB-SEM measured thicknesses could be attributed to three main factors: (1) potential deviations between the assumed nominal density and the actual film density, arising from compositional and structural differences, (2) localized thickness nonuniformities exceeding the FIB-SEM sampling area, and (3) temporal gaps in QMB data acquisition. Despite these uncertainties, the results demonstrate that QMB diagnostics remain a reliable tool for tracking B-based film evolution.

3.4.3. Deuterium retention. The incomplete erosion of B-based films observed in MSA raises critical concerns about hydrogen isotope retention, which warrants further investigation. TDS measurements were performed on the C-QMB working sensor after the campaign, with a specific focus on HD and D_2 desorption to assess D retention behavior.

Figure 13 presents the D desorption profiles for the sensor. Four distinct D desorption peaks were observed at characteristic temperatures of 515 K, 680 K, 830 K, and 950 K, which are likely from the desorption of B-D-B, B-D, B-O-D, and B-C-D, respectively [60–62, 69–71], consistent with bonding states identified by XPS analysis. These primary desorption channels accounted for approximately 95% of the total deuterium release. Two additional minor features near 1100 K and 1220 K are likely attributed to release from void structures [72]. Integration of the complete desorption spectrum yielded a total deuterium retention of 2.12×10^{20} m^{-2} for the C-QMB, which is approximately one order of magnitude lower than the 1.5×10^{21} m^{-2} reported for carbon-dominated mixed materials (B/C ∼0.57) in MSAs on Globus-M [16]. This reduction is attributed to the lower carbon content (B/C = 3.6) observed in this study. Previous results from various tokamak experiments have consistently demonstrated that carbon-rich surfaces retain more D than B-dominated ones, with B-C-D complexes exhibiting notable thermal stability up to 950 K [60, 73]. These findings suggest that limiting carbon incorporation into boron films is an effective strategy for reducing hydrogen isotope retention in fusion devices.

However, the D retention measured here is 8.25 times higher than that observed in a pure W sample located near the main limiter, which was exposed to a 2 hour, 1.6 kW D_2-GDC treatment followed by 20 cycles (180 s) of EAST's 1.2 MW single-configuration discharge. This elevated retention is also consistent with previous measurements (3.23×10^{20} m^{-2}) in ∼75 nm boron–carbon films under similar plasma conditions [43], highlighting the enhanced isotope trapping capacity of shadowed regions. It should also be noted that the presence of B_2O_3, as identified by XPS, may contribute to the formation and release of deuterated water (D_2O) during the TDS process, which could result in an underestimation of the actual deuterium retention. In addition, under high-temperature plasma conditions, the release of D_2O may potentially affect steady-state plasma operations. Therefore, the role of B-C-O film-related desorption processes warrants further investigation in future campaigns [74].

Quantitative evaluation of the D/B ratio was based on a film thickness of 30 nm, a density of 1.6 g × cm^{-3}, and an average boron atomic percentage of 43.08 at% obtained from XPS. This yielded a B surface density of 6.25×10^{20} atoms m^{-2}. Considering the D content measured by TDS, the corresponding D/B ratio was calculated to be 0.34. However, as XPS does not detect D, the B fraction is likely to be overestimated. To better approximate the actual D/B ratio, we assumed a D concentration of ∼30 at%, which is consistent with previous experimental and simulation studies reporting saturation levels of approximately 28–43 at% in boron-containing co-deposits [75–77]. Notably, our XPS measurements indicate a higher boron content and lower carbon content compared to these references, which may influence the achievable deuterium retention. Therefore, the adopted value of ∼30 at% represents a conservative and reasonable estimate for our experimental conditions, under which the actual D/B ratio could approach 0.44. Non-uniform boron deposition and differences in local plasma conditions may lead to localized areas with

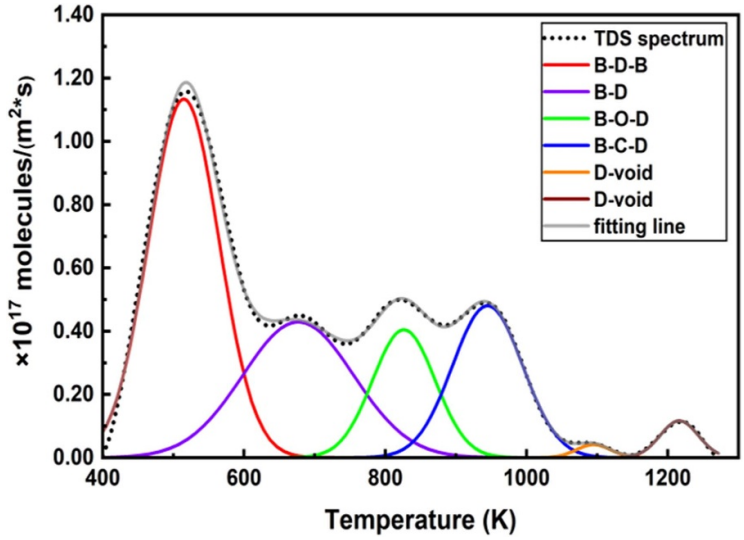

Figure 13. The D TDS spectra for working sensor after the 2024 spring campaign in EAST (the ramping rate during the TDS measurement was 10 °C min^{-1}).

D/B ratios exceeding 0.5 [77], surpassing the conservative upper limit assumed by ITER, where a fixed H/D/T-to-B ratio of 0.5 is used to estimate fuel retention in B co-deposits [10]. The relatively higher D retention observed in shadowed areas underscores the need for effective removal or control strategies for B-containing films in such regions [78, 79]. Furthermore, the D/B ratio measured in EAST is about twice that reported in TEXTOR (∼0.2) for a-B:D layers deposited on the W side of the limiter surface, where diborane was used as the boronization precursor [80]. This observation suggests that diborane, which has also been selected for ITER, may result in lower D retention compared to carborane.

4. Conclusion and outlook

The development of a QMB system at the mid-plane of port C has enabled the measurement of material erosion and deposition during the EAST 2024 spring campaign. This work first systematically analyzes the boron erosion and deposition evolution behavior in MSA under the metal wall configuration.

4.1. Conclusion

The main conclusions are summarized as follows:

(1) Material erosion was observed in 69% of normal and 61% of disruptive discharges, with most mass changes remaining below 6.2 ng cm^{-2}. The predominant erosion observed during disruptions is likely due to the higher reflection coefficient of W. In contrast, routine overnight wall conditioning led to net deposition, with an average accumulation of 0.1 μg cm^{-2} per cleaning. The B-based film on C-QMB exhibited an average erosion rate of 0.19 ng cm^{-2} s^{-1} and a coating lifetime of $\sim 10^4$ s following a single boronization with 10 g carborane, about five times longer than that on the FW.

(2) Boronization effectively reduced impurity levels and mitigated both core and boundary radiation. The observed erosion-to-deposition transition of the C-QMB provides valuable insights into the degradation of B-based films on nearby PFCs. This transition could serve as an indirect diagnostic tool for assessing local boron film lifetime and offer useful information for improving material migration modeling and optimizing wall conditioning strategies to sustain impurity control and plasma performance.

(3) ECRH discharges resulted in erosion rates 1.95 times higher than those in LHW + ECRH discharges. Interestingly, increasing heating power did not lead to an increase in erosion rates, highlighting the critical role of low-energy neutral particles and the importance of heating configuration.

(4) Carbon–boron films formed during boronization underwent significant modification through long-term plasma wall interactions, causing intermixing with PFCs. The C-QMB surface exhibited a hazy morphology, with B concentrations ranging from 29.9 to 44.9 at%. Significant oxygen gettering was observed (O/B ratio ∼0.8), along with a B/C ratio of approximately 3.6. Trace impurities were also identified, including Fe (2.5–6.2 at%) from nearby stainless-steel diagnostic structures and Cu (1.1–2.8 at%) from the LHW antenna.

(5) After the whole campaign, approximately 30 nm of mixed B-based film remained on C-QMB, resulting in a D retention of 2.12×10^{20} m^{-2}, which is 8.25 times higher than that on pure W. This underscores the significant impact of B-rich films on hydrogen isotope retention, particularly in MSAs. The measured D/B ratio (0.34–0.44) on C-QMB was about twice the value (∼0.2) reported in TEXTOR, where diborane was used as the boronization precursor.

4.2. Outlook

In ITER, the full W wall configuration is expected to significantly reduce impurity deposition, particularly from elements such as Fe and Cu, which contributed to mixed-material layers in shadowed areas in EAST. The relatively high B/C ratio observed in EAST helped to suppress D trapping compared to carbon-rich films in Globus-M with a carbon wall, highlighting the importance of using metallic PFCs for hydrogen isotope inventory control. Moreover, the replacement of carborane with diborane as the boronization precursor is likely to decrease D retention.

However, several challenges remain. Due to the net deposition caused by routine wall conditioning, incorporating protective measures such as shutters and *in-situ* cleaning systems for components like diagnostic mirrors will be essential to maintain diagnostic accuracy. ECRH, which is planned for plasma startup in ITER, was found to enhance erosion in EAST under low fueling conditions. This enhancement is likely driven by neutral-induced mechanisms, although the specific mechanisms are not yet fully understood and require further investigation. The impact could be more severe in ITER, emphasizing the necessity of carefully assessing neutral particle effects during ECRH operation to avoid unexpected PFC degradation. Additionally, the extended lifetime of boron films observed in shadowed areas in EAST suggests that long-term material retention may also occur in ITER, raising concerns regarding hydrogen isotope inventory management and the potential for flake detachment that could trigger plasma disruptions. To better predict and mitigate such risks, future work will incorporate modeling approaches such as WallDYN or ERO, combined with EAST experimental data, to enable cross-validation and improve understanding of material migration and retention behaviors.

Acknowledgment

This work was supported by the National key R&D project of China with project number of 2024YFE03000200, 2022YFE03030000, and 2024YFE03160004, the National Nature Science Foundation of China under Contract Nos. 12275306, 11975269, U24A2020, and 12075279, the Youth Innovation Promotion Association of Chinese Academy of Sciences under certificate No. 2022452, the Anhui Provincial Natural Science Foundation under contract No. 2208085J40, the Anhui Provincial Major Science and Technology Project under contract No. E35AH205B3, the CASHIPS Director's Fund with Grant Nos. BJPY2023B03, YZJJQY202302, and BJPY2023A03, and the Comprehensive Research Facility for Fusion Technology Program of China with Grant No. 2018-000052-73-01-001228. We gratefully thank the vacuum group members at EAST for their valuable support and Dr Volker Rohde for his insightful discussions and guidance. We also thank the staff members at EAST (https://cstr.cn/31130.02.EAST), for providing technical support and assistance in data collection and analysis.

ORCID iDs

Zichao Lin 0000-0002-2417-8191
Andrey Litnovsky 0000-0001-9791-4316

References

[1] Gao B.F., Ding R., Xie H., Zeng L., Zhang L., Wang B., Li C., Zhu D., Yan R. and Chen J. 2020 Plasma-facing components damage and its effects on plasma performance in EAST tokamak *Fusion Eng. Des.* **156** 111616
[2] Winter J. *et al* 1989 Boronization in TEXTOR *J. Nucl. Mater.* **162–164** 713–23
[3] Goriaev A., Wauters T., Brakel R., Brezinsek S., Dinklage A., Fellinger J., Grote H., Moseev D., Sereda S. and Volzke O. 2020 Wall conditioning at the Wendelstein 7-X stellarator operating with a graphite divertor *Phys. Scr.* **T171** 014063
[4] Bedoya F., Allain J.P., Scotti F., LaBombard B., Kaita R. and Krstic P.S. 2018 Effect of boronization on plasma-facing graphite surfaces and its correlation with the plasma behavior in NSTX-U *Nucl. Mater. Energy* **17** 211–6
[5] Lipschultz B. *et al* 2007 Influence of boronization on operation with high-Z plasma facing components in Alcator C-Mod *J. Nucl. Mater.* **363–365** 1110–8
[6] Scott S. *et al* 2007 Overview of the Alcator C-MOD research programme *Nucl. Fusion* **47** S598–S607
[7] Apicella M.L., Mazzitelli G., Esposito B., Gabellieri L., Leigheb M., Ridolfini V.P., Pieroni L., Romanelli M. and Zagórski R. (FTU Team) 2005 Effects of wall boron coating on FTU, an all metallic and carbon free medium size tokamak *Nucl. Fusion* **45** 685–93
[8] Kallenbach A. *et al* 2009 Non-boronized compared with boronized operation of ASDEX Upgrade with full-tungsten plasma facing components *Nucl. Fusion* **49** 045007
[9] Yang J., Hong S.H., Kim D., Jang J., Kim J.Y., Jung E.C., Kim Y. and Hwang Y.S. 2018 Effect of boronization in VEST: achieving 0.1 MA discharge *Fusion Eng. Des.* **137** 358–61
[10] Pitts R.A. *et al* 2025 Plasma-wall interaction impact of the ITER re-baseline *Nucl. Mater. Energy* **42** 101854
[11] Hakola A., Likonen J., Koivuranta S., Krieger K., Mayer M., Neu R., Rohde V. and Sugiyama K. 2011 Global transport of light elements boron and carbon in the full-W ASDEX Upgrade *J. Nucl. Mater.* **415** S227–S30
[12] Schustereder W., Herrmann A. and Rohde V. 2007 Impurity survey after boronization in ASDEX Upgrade measured by a collector probe *Phys. Scr.* **T128** 14–17
[13] Tramontin L., Antoni V., Bagatin M., Boscarino D., Cattaruzza E., Rigato V. and Zandolin S. 1999 Erosion, redeposition and boronization lifetime in RFX *J. Nucl. Mater.* **266–269** 709–13
[14] Ghezzi F. and Tolstogouzov A. 2008 Boron deposition on the graphite tiles of the RFX device studied by secondary ion mass spectrometry *J. Nucl. Mater.* **373** 402–6
[15] Ghezzi F., Laguardia L., Caniello R., Canton A., Dal Bello S., Rais B. and Anderle M. 2015 Erosion, XPS, SIMS and FTIR-ATR characterization of boronized graphite from the thermonuclear plasma device RFX-mod *Appl. Surf. Sci.* **345** 408–19
[16] Gusev V.K. *et al* 2009 In-vessel surface layer evolution during plasma-wall interaction in the Globus-M spherical tokamak *Nucl. Fusion* **49** 095022
[17] Kreter A., Wienhold P., Esser H.G., Litnovsky A., Philipps V. and Sugiyama K. 2013 Long-term carbon transport and fuel

retention in gaps of the main toroidal limiter in TEXTOR *J. Nucl. Mater.* **438** S746–S9
[18] Widdowson A. *et al* 2021 Evaluation of tritium retention in plasma facing components during JET tritium operations *Phys. Scr.* **96** 124075
[19] Stangeby P.C. *et al* 2022 Developing solid-surface plasma facing components for pilot plants and reactors with replenishable wall claddings and continuous surface conditioning. Part A: concepts and questions *Plasma Phys. Control. Fusion* **64** 055018
[20] Skinner C.H., Roquemore A.L., Bader A. and Wampler W.R. (the NSTX Team) 2004 Deposition diagnostics for next-step devices (invited) *Rev. Sci. Instrum.* **75** 4213–8
[21] Ochoukov R., Whyte D., Lipschultz B., LaBombard B., Gierse N. and Harrison S. 2012 Study and optimization of boronization in Alcator C-Mod using the Surface Science Station (S^3) *Fusion Eng. Des.* **87** 1700–7
[22] Skinner C.H., Kugel H.W., Roquemore A.L., Maingi R. and Wampler W.R. 2007 Pulse-by-pulse measurements of dynamic retention and deposition in NSTX *J. Nucl. Mater.* **363–365** 247–51
[23] Kreter A., Esser H.G., Brezinsek S., Coad J.P., Kirschner A., Fundamenski W., Philipps V., Pitts R.A. and Widdowson A. 2009 Nonlinear impact of edge localized modes on carbon erosion in the divertor of the JET tokamak *Phys. Rev. Lett.* **102** 045007
[24] Zhang Y., Peng J., Ding R., Xie H., Mu L. and Chen J.L. 2020 Development of a quartz crystal microbalance diagnostic for measuring material erosion and deposition on the first wall in EAST *Rev. Sci. Instrum.* **91** 076101
[25] Wu J.H., Hu J.S., Chen Y., Ashikawa N., Yu Y.W., Li J.H., Zuo G.Z., Wang X.M., Zhao Y.P. and Li J.G. 2011 Recent results of boronization on EAST and HT-7 superconducting tokamak *J. Nucl. Mater.* **415** S1046–S9
[26] Li J.G. *et al* 1999 ICRF boronization—a new technique towards high efficiency wall coating for superconducting tokamak reactors *Nucl. Fusion* **39** 973
[27] Liu Y.M. *et al* 2024 Studies of the material erosion and deposition during the wall conditioning processes using quartz crystal microbalance in EAST *Nucl. Mater. Energy* **38** 101576
[28] Mu L. *et al* 2022 Studies of aluminum erosion by neutral particles using quartz crystal microbalance and low energy neutral particle analyzer on EAST *Nucl. Mater. Energy* **33** 101248
[29] Song Y.T. *et al* 2022 Recent EAST experimental results and systems upgrade in support of long-pulse steady-state plasma operation *IEEE Trans. Plasma Sci.* **50** 4330
[30] Sauerbrey G.Z. 1959 Verwendung von Schwingquarzen zur Wägung dünner Schichten und zur Mikrowägung *Z. Phys.* **155** 206–22
[31] Zhang Y., Peng J., Ding R., Xie H., Yan R., Mu L. and Chen J.L. 2021 Real time monitoring of material erosion and deposition for the first wall using quartz crystal microbalance in EAST *Nucl. Mater. Energy* **26** 100877
[32] Kawakami R. and Ohya K. 2001 Comparison between static and dynamic simulations of ion reflection and sputtering from layered materials *Jpn. J. Appl. Phys.* **40** 5399
[33] Long Q., Xu G., Ding R., Wang H., Zhang Y., Hai R., Bai X., Gao B. and Chen J. 2024 Study of deuterium reflection on tungsten material with lithium coating in EAST tokamak *Nucl. Mater. Energy* **41** 101840
[34] Loarte A. *et al* 2007 Transient heat loads in current fusion experiments, extrapolation to ITER and consequences for its operation *Phys. Scr.* **T128** 222–8
[35] Jepu I. *et al* 2024 Overview of damage to beryllium limiters by unmitigated disruptions and runaway electrons in the JET tokamak with metal walls *Nucl. Fusion* **64** 106047
[36] Gaspar J. *et al* 2024 Thermal and statistical analysis of the high-Z tungsten-based UFOs observed during the first deuterium high fluence campaign of the WEST tokamak *Nucl. Mater. Energy* **41** 101745
[37] Wauters T., Hagelaar G.J.M. and Pitts R.A. 2025 Modeling input to the ITER glow discharge boronization system design *Nucl. Mater. Energy* **42** 101891
[38] Liu Y.M. *et al* 2025 Studies of material deposition during boronization using quartz crystal microbalance in EAST *Nucl. Mater. Energy* **44** 101964
[39] Cheng Y.X. *et al* 2024 Experimental study on metallic impurity behavior with boronization wall conditioning in EAST tokamak *Nucl. Mater. Energy* **41** 101744
[40] Schmid K. and Wauters T. 2024 Full W ITER: assessment of expected W erosion and implications of boronization on fuel retention *Nucl. Mater. Energy* **41** 101789
[41] Kim B., Seon C., Oh S.-G., Kim Y.K., An Y., Bang E., Hong S.-H., Pak S., Cheon M. and Lee H.G. 2018 A passive mitigation strategy of impurity deposition on the first mirrors using duct with baffles: a case study at a port of KSTAR with *in-situ* deposition monitoring *Fusion Eng. Des.* **129** 269–76
[42] Litnovsky A. *et al* 2019 Diagnostic mirrors for ITER: research in the frame of International Tokamak Physics Activity *Nucl. Fusion* **59** 066029
[43] Puyang S.A., Xu Y.P., Guan Y.H., Yang Z.S., Ding F., Zhou H.S., Zuo G.Z., Hu J.S. and Luo G.-N. 2024 Evolution of hydrogen isotopes retention behavior of *in-situ* boronization films in EAST *Nucl. Fusion* **64** 074001
[44] Giruzzi G. *et al* 2009 Investigation of steady-state tokamak issues by long pulse experiments on Tore Supra *Nucl. Fusion* **49** 104010
[45] de la Cal E. *et al* 2025 Particle fluxes and gross erosion at limiters in JET low-confinement mode plasmas measured with visible cameras *Nucl. Fusion* **65** 046021
[46] Chankin A.V., Coster D.P. and Dux R. 2014 Monte Carlo simulations of tungsten redeposition at the divertor target *Plasma Phys. Control. Fusion* **56** 025003
[47] Ding R. *et al* 2016 Simulation of gross and net erosion of high-Z materials in the DIII-D divertor *Nucl. Fusion* **56** 016021
[48] Zheng W., Yan R., Ding R., Gao B., Wang B., Chen J., Liu N., Zhang Y., Si X. and Zi P. 2022 Studies of material deposition on the graphite divertor tile after the 2019 experimental campaign in EAST *Nucl. Mater. Energy* **33** 101252
[49] Mense A.T., Houlberg W.A., Attenberger S.E. and Milora S.L. 1979 Effects of fueling profiles on plasma transport *Nucl. Fusion* **19** 1473
[50] Colchin R.J. and Owen L.W. 2003 Neutral particle fueling at the midplane of DIII-D *J. Nucl. Mater.* **313–316** 609–13
[51] Voss D.E. and Cohen S.A. 1982 Lowenergy neutral atom spectrometer *Rev. Sci. Instrum.* **53** 1696
[52] Liu N.X., Mu L., Ding R., Zhu Y.B., Li S., Xie H., Yan R., Peng J. and Chen J.L. 2021 Measurements of neutral particle energy spectrum on EAST using a time-of-flight low-energy neutral particle analyzer *Rev. Sci. Instrum.* **92** 063507
[53] Tendler M. and Heifetz D. 1987 Neutral particle kinetics in fusion devices *Fusion Sci. Technol.* **11** 289–310
[54] Verbeek H., Stober J., Coster D.P., Eckstein W. and Schneider R. 1998 Interaction of charge exchange neutrals with the main chamber walls of plasma machines *Nucl. Fusion* **38** 1789
[55] Rimini F.G. and Saibene G. (JET Team) 2002 Core and edge confinement studies with different heating methods in JET *Nucl. Fusion* **42** 86–93

[56] Barabaschi P., Fossen A., Loarte A., Becoulet A. and Coblentz L. 2025 ITER progresses into new baseline *Fusion Eng. Des.* **215** 114990
[57] Sharapov V.M. 2021 Discharge chamber plasma-chemical conditioning in magnetic confinement fusion devices (Review) *Phys. At. Nucl.* **84** 1266–71
[58] Min Z., Xiao-dong Z. and Xue-mao G. (HT-7 PSI group) 2000 XPS Analysis of a-B/C:H film deposited by ICRF boronization *Plasma Sci. Technol.* **2** 317–22
[59] Shao D.D., Li J., Tan X., Yang Z., Okuno K. and Oya Y. 2015 XPS investigation of impurities containing boron films affected by energetic deuterium implantation and thermal desorption *J. Nucl. Mater.* **457** 118–23
[60] Abe S. *et al* 2025 Deuterium retention behaviors of boronization films at DIII-D divertor surface *Nucl. Mater. Energy* **42** 101855
[61] Yang Z.S., Wang W., Li Q., Wu J., Okuno K., Oya Y. and Luo G.-N. 2011 Surface analysis of VPS-W coatings boronized by an ICRF discharge in HT-7 *J. Nucl. Mater.* **417** 520–3
[62] Yoshikawa A., Kikuchi Y., Suda T., Ashikawa N., Nishimura K., Sagara A., Noda N., Oya Y. and Okuno K. 2009 Chemical behavior of hydrogen isotopes into boronized film in LHD *J. Nucl. Mater.* **386–388** 367–70
[63] Yoshikawa A., Oyaidzu M., Miyauchi H., Oya Y., Sagara A., Noda N. and Okuno K. 2007 Effect of oxygen concentration on the chemical behavior of deuterium implanted into oxygen-containing boron thin films *J. Nucl. Mater.* **367–370** 1527–30
[64] Sharapov V.M., Mirnov S.V., Grashin S.A., Lebedev S.V., Kovan I.A., Krasilnikov A.V., Krupin V.A., Levin L.S., Romannikov A.N. and Zakharov A.P. 1995 Boronization of Russian tokamaks from carborane precursors *J. Nucl. Mater.* **220–222** 730–5
[65] Alimov V.K. *et al* 1992 Characterization of a-B/C:H films deposited from different boron containing precursors *J. Nucl. Mater.* **196–198** 670–5
[66] Mayer M. *et al* 2024 Properties of boron layers deposited during boronisations in W7-X *Nucl. Mater. Energy* **41** 101778
[67] Skinner C.H., Kugel H., Roquemore A.L., Hogan J. and Wampler W.R. 2005 Time resolved deposition measurements in NSTX *J. Nucl. Mater.* **337–339** 129–33
[68] Skinner C.H., Bedoya F., Scotti F., Allain J.P., Blanchard W., Cai D., Jaworski M. and Koel B.E. 2017 Advances in boronization on NSTX-Upgrade *Nucl. Mater. Energy* **12** 744–8
[69] Suzuki M., Kurata R., Kobayashi M., Ashikawa N., Sagara A., Oya Y. and Okuno K. 2011 Retention behaviors of hydrogen isotope in boron film exposed to H-H discharge in LHD *J. Nucl. Mater.* **415** S728
[70] Matsuoka K., Kobayashi M., Kurata R., Osuo J., Ashikawa N., Sagara A., Oya Y. and Okuno K. 2011 Impurity effects on hydrogen isotope retention in carbon-oxygen containing boron films *Fusion Sci. Technol.* **60** 412–6
[71] Oya Y., Kodama H., Oyaidzu M., Morimoto Y., Matsuyama M., Sagara A., Noda N. and Okuno K. 2004 Implanted hydrogen isotope retention and chemical behavior in boron thin films for wall conditioning *J. Nucl. Mater.* **329–333** 870–3
[72] De Temmerman G. and Doerner R.P. 2009 Deuterium retention and release in tungsten co-deposited layers *J. Nucl. Mater.* **389** 479–83
[73] Suzuki S., Yang Y., Yoshikawa A., Kikuchi Y., Sagara A., Oya Y. and Okuno K. 2009 Influence of carbon concentration on chemical behavior of energetic deuterium implanted into carbon-contained boron film *J. Nucl. Mater.* **390–391** 200–2
[74] Okuno K., Suzuki S., Kobayashi M., Kurata R., Masao M., Ashikawa N., Sagara A. and Oya Y. 2010 Retention behavior of hydrogen isotopes in boron film deposited on SS-316 for LHD first wall *Fusion Eng. Des.* **85** 2328–30
[75] Mayer M., Rohde V., Ramos G., Vainonen-Ahlgren E., Likonen J., Herrmann A. and Neu R. 2007 The deuterium inventory in ASDEX Upgrade *Nucl. Fusion* **47** 1607–17
[76] Domínguez-Gutiérrez F.J., Bedoya F., Krstic P.S., Allain J.P., Neff A.L. and Luitjohan K. 2017 Studies of lithiumization and boronization of ATJ graphite PFCs in NSTX-U *Nucl. Mater. Energy* **12** 334–40
[77] Bedoya F., Allain J.P., Dominguez-Gutierrez F.J. and Krstic P.S. 2019 Effect of deuterium irradiation on graphite boronized in the NSTX-U tokamak *Sci. Rep.* **9** 2435
[78] Roche H., Delaporte P., Grisolia C., Languille P., Loarer T., Martin C., Panayotis S., Pascal J.-Y., Pégourié B. and Tsitrone E. 2013 Layer removal in gaps by laser process *J. Nucl. Mater.* **438** S1079–S83
[79] Litnovsky A. *et al* 2011 Overview of material migration and mixing, fuel retention and cleaning of ITER-like castellated structures in TEXTOR *J. Nucl. Mater.* **415** S289–S92
[80] Huber A., Mayer M., Philipps V., Pospieszczyk A., Ohgo T., Rubel M., Schweer B., Sergienko G. and Tanabe T. 2001 *In-situ* measurement of trapped hydrogen by laser desorption in TEXTOR-94 *Phys. Scr.* **T94** 102–5